Impact of organic molecule rotation on the optoelectronic properties of hybrid halide perovskites

Qiaoling Xu,[1,2] Alessandro Stroppa,[3] Jian Lv,[1] Xingang Zhao,[1] Dongwen Yang,[1] Koushik Biswas,[4] and Lijun Zhang[1,*]

[1]*Key Laboratory of Automobile Materials of MOE, and School of Materials Science and Engineering, Jilin University, Changchun 130012, China*

[2]*Center for Computational Sciences, Sichuan Normal University, Chengdu, 610068, China*

[3]*CNR-SPIN, c/o Dip.to di Scienze Fisiche e Chimiche - Via Vetoio - 67100 - Coppito (AQ), Italy*

[4]*Department of Chemistry and Physics, Arkansas State University, State University, Arkansas 72467, USA*

(Received 3 February 2019; revised manuscript received 27 August 2019; published 3 December 2019)

The importance of organic molecular cation orientation and interaction with surrounding inorganic framework in the optoelectronic hybrid halide perovskites is a topic of considerable interest. To that end, we study the effect of organic molecule rotations on the properties of such hybrid semiconductors using the swarm intelligence-based structure prediction method combined with *ab initio* density functional calculations. Adopting the cubic phases of $APbI_3$ [A = CH_3NH_3(MA), $CHNH_2NH_2$(FA) and $CH_3CH_2NH_3$(EA)], we determine the energetically stable/metastable configurations of organic molecules inside the quasicubic perovskite cages. Different cation orientations result in up to ∼250 meV/formula changes in the material free energy, reflecting the complex energy landscape of these hybrid materials containing dynamically rotating organic components. Notably, the [012] orientation of MA is found to give the most stable structure of $MAPbI_3$, while the conventional [001], [011], or [111] directions remain slightly higher in energy. Molecular orientations clearly influence the fundamental electronic bandgap and also modify the magnitude of Rashba-type energy band splitting resulting in indirect gap behavior. However, the dielectric screening remains large for all orientations thus creating weakly bound excitons. Based on the analysis of many organic molecule configurations obtained through the structure search technique, our results provide insightful understanding on the effects of organic molecule rotation on optoelectronic properties and carrier dynamics of hybrid halide perovskites.

DOI: 10.1103/PhysRevMaterials.3.125401

I. INTRODUCTION

Photovoltaic (PV) devices based on hybrid lead-halide perovskites have quickly reached a certified power conversion efficiency of above 25% [1], rivaling that of the more traditional and widely investigated solar cell materials. Great attention has been considered for their fundamental properties that impact PV performances [2–4]. These materials feature a unique set of characteristics: tunable band gaps [5], strong optical absorption [6,7], long carrier lifetime and diffusion lengths [8–11], weak exciton binding energy [12–25], and tolerance towards deep defects [26–29]. The underlying physical mechanisms responsible for these advantageous properties continue to be a topic of investigation.

The orientation of the organic dipoles embedded within the cubo-octahedral cavity formed by the lead-halide octahedral network, represent a subtle condition in the geometrical configuration of hybrid perovskites. It is believed that hybrid perovskites are dynamical materials where the dipole orientations and concerted octahedral tilting introduce a level of disorder in the crystals. Although X-ray diffraction can distinguish the different crystalline phases of hybrid perovskites, it does not provide full information on the position and orientation of the organic molecules relative to the inorganic framework. There is, however, additional experimental evidence that strongly favor orientational disorder among the organic cations [30–41]. Many computational studies have also addressed rotational motion, reorientation dynamics, and their effects on the electronic properties [31,33,34,42–46]. It has been suggested that the molecules may behave as nearly free rotors in the room-temperature tetragonal and high-temperature cubic phases of $MAPbI_3$ [47,48]. Even though the organic cations in cubic $MAPbI_3$ are highly disordered, their orientations can still be considered discrete. Onoda-Yamamuro *et al.* proposed three models based on thermal analysis which describes discrete molecular orientations with the C-N axis directed towards the face [100], edge [110], and corner [111] of cubic $MAPbI_3$ [30]. Other reports also suggested preferential molecular orientations in cubic [26,45,47,49–56] and tetragonal phase hybrid perovskites [51]. Quasielastic neutron scattering measurements by Leguy *et al.* showed hopping MA rotations where the organic dipoles jump between preferential orientations on a timescale of several picoseconds, ruling out the possibility of free rotations at temperatures below 370 K [38]. At temperatures relevant for solar cell operation one could envisage multiple local minima in the ground-state potential energy surface of hybrid perovskites which are characterized by different molecular orientations resulting in local symmetry breaking [57,58], the instantaneous structure having implications on the electronic properties [58]. Thus, what is observed experimentally is only an average crystal geometry while the material continually distorts, consequent to the organic rotations and associated tilting of the Pb-I octahedra.

*lijun_zhang@jlu.edu.cn

While it is known that the molecular states are not directly involved in the band edges [59], the role of molecular rotations seem to have a strong influence on the inorganic framework, indirectly affecting the electronic and optical response of hybrid perovskites [44,50,54]. Preferential organic orientations locally perturb the Pb-I lattice causing octahedral distortions, leading to variations in the band gap and carrier effective mass, which eventually control charge carrier dynamics and recombination [5,60–62]. A comprehensive look at molecular orientations in hybrid perovskites and how they impact electronic properties is thus very important. This will be the focus of the current study.

To study the importance of molecular orientations in hybrid perovskites, we implemented first-principles particle swarm optimization (PSO) structure search calculations including van der Waals dispersion (vdW) correction. Though both the previous molecular dynamics (MD) calculations [31,39,42–44,63,64] and our work can evaluate the rotation energy barriers of organic molecules, our work may add new aspects: First, the combination of PSO with first-principles calculations allows us to explore numerous structures in the energy landscape of hybrid perovskites. The PSO, in principle, can overcome much larger barriers in the energy landscape more efficiently than the MD approach to obtain possible new orientation of organic molecules. Second, thousands of static electronic structure calculations from structure searches enable us to investigate the extent to which the free energy and materials properties related to optoelectronic application are affected by the molecular reorientations coupled with octahedral tilting. For this study, the cubic phase of $APbI_3$ with three different organic cations [A = CH_3NH_3(MA), $CHNH_2NH_2$(FA), and $CH_3CH_2NH_3$(EA)] are chosen. The generated structures and their electronic properties reveal interesting patterns in the evolution of the band gap (Eg), Rashba band splitting, effective mass, and exciton binding energy. The results indicate variability among these properties, thus emphasizing the important role of the size and orientation of organic molecules.

II. COMPUTATIONAL DETAILS

The preferable orientations of MA, FA, and EA within the PbI_3 framework is explored via PSO algorithm as implemented in the CALYPSO code [65,66]. For instance, the identified stable and metastable structures obtained from a population of candidate solutions of $MAPbI_3$ are shown in Fig. 1.

For the generation of the initial structures we considered the cubic PbI_3 framework, fixing the center of mass of MA, FA, and EA molecules at the ideal A-site and allowing them to rotate freely about C-N or C-C axes as appropriate for the respective cases. The rotation of the organic cations is determined by three degrees of freedom: polar angle (θ), azimuthal angle (ϕ), and spinning angle (ψ), as shown Figs. 1 and S1 in the Supplemental Material [67]. Keeping the same cubic symmetry among the three lead-halide perovskites allows a systematic comparison as the internal geometry and corresponding electronic structure evolve due to organic cation rotations. We note that $FAPbI_3$ and $MAPbI_3$ have been experimentally reported to adopt a cubic structure at 298 and above 327 K, respectively [47,68]. We constrain $EAPbI_3$ in the same structure, although this system was recently reported in the orthorhombic phase having chain-like features with intervening EAs [69].

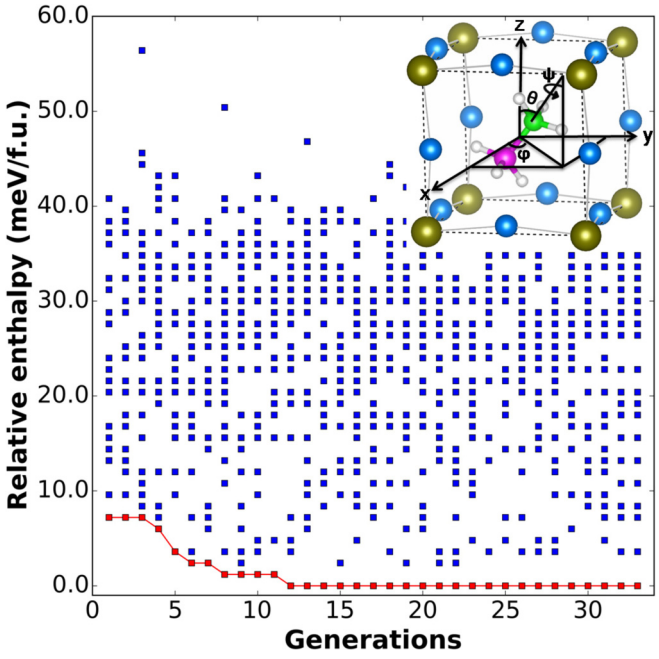

FIG. 1. Relative energy of predicted configurations as a function of generation for the $MAPbI_3$, obtained by the PSO. The inset shows three rotational degrees of freedom [polar angle (θ), azimuthal angle (ϕ), spinning angle (ψ)] of the molecule MA embedded in the framework of PbI_3.

For structure evolution, PSO is used, as a global optimization algorithm, which is inspired by the social behavior of birds flocking or fish schooling. It can be seen as a distributed behavior algorithm that performs a multi-dimensional search. In practice, a candidate structure in the configurational space is regarded as a particle, and a set of individual particles is called a population/generation. Each particle explores the search space via a velocity vector which is affected by both its personal best experience and the best position found by the population thus far. During the process of evolution, the structures satisfy the following equations:

$$x_{ij}^{t+1} = x_{ij}^{t} + v_{ij}^{t+1}, \tag{1}$$

$$v_{ij}^{t+1} = \omega v_{ij}^{t} + c_1 r_1 \left(\text{pbest}_{ij}^{t} - x_{ij}^{t}\right) + c_2 r_2 \left(\text{gbest}_{ij}^{t} - x_{ij}^{t}\right), \tag{2}$$

where i is a structure regarded as a particle in the search space and $j \in \{\theta, \phi, \psi\}$. Equation (1) is used to update the positions of the particles. The new position of each individual i at the jth dimension is calculated based on its previous location (x_{ij}^{t}) before optimization and its new velocity (v_{ij}^{t+1}). The new velocity depends on the previous velocity (v_{ij}^{t}), current location (pbest_{ij}^{t}) with an achieved best fitness of lowest enthalpy of the particle, and the best global fitness value for the entire population (swarm) (gbest_{ij}^{t}), according to Eq. (2). ω denotes the inertia weight and controls the momentum of the particle.

Structure optimization is conducted within the density functional theory (DFT) using the plane-wave pseudopoten-

tial method implemented in the Vienna *Ab initio* Simulation Package (VASP) [70]. The electron-ion interaction is described using projector augmented-wave (PAW) pseudopotentials [71]. The $2s^2 2p^2$ states of C, $2s^2 2p^3$ of N, $2s^2 2p^4$ of O, $1s$ of H, $6s^2 6p^2$ of Pb, and $5s^2 5p^5$ of I are included as valence electrons. We use Perdew, Burke, and Ernzerhof (PBE) [72,73] as the exchange correction functional. An energy cutoff of 470 eV and the mesh of k-points of $6 \times 6 \times 6$ ($MAPbI_3$) and $5 \times 5 \times 5$ ($FAPbI_3$ and $EAPbI_3$) are used for geometry optimization and electronic structure calculations. Convergence tests indicate that the total energy converges at an accuracy of less than 0.1 meV/atom with respect to cutoff energy, and at an accuracy of 0.2 meV/atom with respect to the k-point sampling (Fig. S2) [67]. Long-range dispersion interactions, which play an important role [54,74–76] on organic cation orientation and structure determination, are considered in this work. We compared the equilibrium lattice parameters of $MAPbI_3$ in the cubic phase (see Table S1) [67] and found that both optB86b and optB88b vdW functionals [77] provide better agreement, within about 0.3% of experimental values [47]. The optB86b vdW functional is adopted for all subsequent calculations. To constrain the cubic symmetry, all structures are optimized by fixing cell shape ($a = b = c$), while relaxing their volumes and internal coordinates.

For band-gap calculations of the most stable configurations with favored molecular orientations, we used hybrid functional (HSE) [78] with adjustable Fock exchange (given by mixing parameter $\alpha = 55\%$) [79] and including spin-orbit coupling (SOC). The calculated results show reasonable agreement with available experimental data as shown below. We also found that the band gaps from the HSE + SOC approach are very close to the DFT-PBE derived values, as demonstrated in Fig. 2. This has been reported in literature [26], i.e., neglecting the SOC effect leads to fortuitous agreement between calculated DFT-PBE and experimental band gaps of hybrid halide perovskites. Thus, we used the DFT-PBE approach to obtain fairly accurate band-gap estimates of thousands of searched structures caused by reorientation of the organic molecules. We used the DFT-PBE approach, including SOC, to calculate the Rashba-type splitting near the band edges, which is caused by broken inversion symmetry associated with molecular orientations.

We also used the BOLTZTRAP code [80] to calculate carrier effective mass (m^*) tensors with a dense k-point grid of $10 \times 10 \times 10$ and unified carrier concentration of 1.0×10^{18} cm^{-3} at temperature of 300 K. We calculated carrier effective masses of stable configurations with the favored molecular orientations by using the DFT-PBE approach with and without the SOC effect, as shown in supplementary Table S2 [67]. For the three hybrid perovskites, the hole effective masses remain almost unaffected by the SOC, while the electron masses were uniformly overestimated by the DFT-PBE approach without the SOC. This is expected since the SOC mainly affects the Pb-p orbitals dominating conduction bands, but has no impact on the valence bands derived from Pb-s states (where the relativistic Darwin effect causes the energy level upshift). For thousands of searched structures caused by the reorientation of organic molecules, our goal is to explore the extent to which the carrier effective masses are affected by the molecular

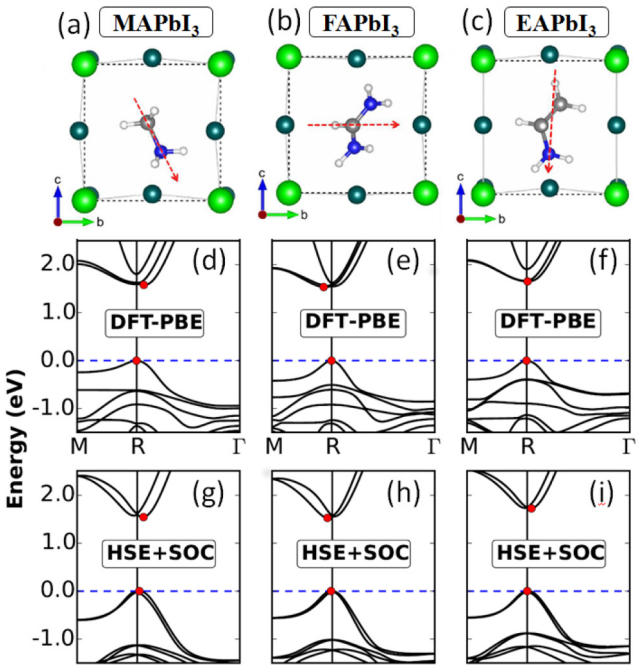

FIG. 2. The predicted stable structures and calculated corresponding band structures using PBE and HSE (with adjustable Fock exchange, given by mixing parameter $\alpha = 55\%$) + SOC functional, respectively, for (a), (d), (g) $MAPbI_3$, (b), (e), (h) $FAPbI_3$, and (c), (f), (i) $EAPbI_3$. Note that the MA is directed to the orientation [012].

reorientations coupled with octahedral tilting. Considering the computational cost of the effective mass calculations needing dense k-point grid when the SOC is included, we employed the DFT-PBE approach w/o SOC for such calculations. As such, we note that our calculated effective masses of conduction electrons are clearly overestimated. Then, an estimation of the binding energy (E_B) of the hydrogenic Wannier-Mott exciton is made, using $E_B = \mu R_y / m_0 \epsilon_\infty^2$, where μ is the reduced carrier effective mass ($1/\mu = 1/m_e^* + 1/m_h^*$), ϵ_∞ is the calculated high-frequency dielectric constant obtained by purturbation theory within PBE and R_y is the atomic Rydberg energy.

III. RESULTS AND DISCUSSION

As shown in Figs. 1 and S1, different cation orientations result in up to ~60 meV/formula for $MAPbI_3$, ~150 meV/formula for $FAPbI_3$, and ~250 meV/formula for $EAPbI_3$ changes in the ground-state total energy. This reflects the complex energy landscape of these hybrid materials containing dynamically rotating organic components. Figures 2(a)–2(c) shows the favored molecular orientation in the predicted stable configurations of the three compounds: $MAPbI_3$, $FAPbI_3$, and $EAPbI_3$ (structural details are summarized in Table S3) [67]. Corresponding lattice parameters are 6.310 Å (experiment: 6.328 Å [47]), 6.370 Å (experiment: 6.362 Å [68]), and 6.418 Å for $MAPbI_3$, $FAPbI_3$, and $EAPbI_3$, consistent with the increasing size of the organic cations MA^+, EA^+, FA^+. The arrows in Fig. 2 represent molecular dipole moments. It is interesting to note that the C-N axis of MA^+ is directed along [012] with Pm symmetry in the

predicted lowest energy configuration of $MAPbI_3$ cubic unit cell; deviating from the conventional [100], [45,50–53] [110], [49,54] and [111] directions [26,55,56]) which are commonly cited in the literature. The calculated total energies of [110], [001], and [111] orientations are higher than that of [012] by 16, 26, 45 meV/formula unit, respectively. In case of $FAPbI_3$, it has been suggested that the C-H bond of FA^+ is directed towards a cube face [100], thus minimizing the (C-H)$\cdots$I interactions while the C-Ns are oriented in a way that allow (N-H)$\cdots$I hydrogen bonds [68]. Our structure search predicts a different $FAPbI_3$ ground state where the N-CH-N part of FA lies approximately within the (111) plane, distinct from the FA lying in the (200) plane in Ref. [68]. We find this configuration of $FAPbI_3$ to be more stable, by about 124 meV/formula unit, compared to the one where the C-H bond is directed along [100]. The preferred molecular orientations in $MAPbI_3$ and $FAPbI_3$ predicted by the structure search approach potentially means increased hydrogen bonding [(N-H)$\cdots$I bonds] in the distorted, pseudocubic hosts—emphasizing the interplay between organic motifs and inorganic framework in these dynamical materials. Relatively small energy differences between specific configurations also imply that the molecules may be rotationally mobile at room temperature, i.e., their orientations continue to evolve due to rotor-like or tumbling motion, without the possibility of long-range ferroelectric ordering.

The electronic band structures of $MAPbI_3$, $FAPbI_3$, and $EAPbI_3$ stable configurations are shown in Fig. 2. As is well known in the case of hybrid perovskites, neglecting spin-orbit effects leads to fortuitous agreement between calculated PBE band gaps (Eg) and experimental values. Nevertheless, it provides reasonable estimates as evident from the comparison to the results calculated by the HSE + SOC functional with adjustable Fock exchange (given by mixing parameter $\alpha = 55\%$), shown in Fig. 2. However, band splitting and band-edge position relative to the core levels are more accurately described when spin-orbit coupling and nonlocal exchange interaction is included as in the case of HSE + SOC. The calculated HSE + SOC gaps are 1.54, 1.52, 1.72 eV for $MAPbI_3$, $FAPbI_3$, and $EAPbI_3$ following the trend: Eg (FA) < Eg (MA) < Eg(EA), which is in reasonable agreement with available experimental results: ~1.5-1.7 eV in $MAPbI_3$ [81–88] and 1.43-1.48 eV in $FAPbI_3$ [61,89–91]. All structures show an indirect band gap near the high symmetry *R* point as indicated in Fig. 2.

Next, we describe the "dynamical band gap" behavior caused by molecular reorientations coupled with octahedral tilting as obtained from our search. For example, in the case of $MAPbI_3$ the HSE + SOC calculated band-gap changes from 1.54 eV in the preferred [012] organic orientation (most stable structure) to about 1.47 eV when cations are directed along [111]. Figure 3 shows band-gap variations of the searched structures in all three compounds caused by reorientation of the differently sized organic cations and corresponding distortions of the Pb-I octahedral framework [92]. The presented gap values are based on PBE functional without spin-orbit coupling and plotted as a function of relative energy w.r.t the most stable structure. In a previous study, Mosconi *et al.* investigated the dynamics of organic rotations, observing that the highest occupied molecular orbital (HOMO) level

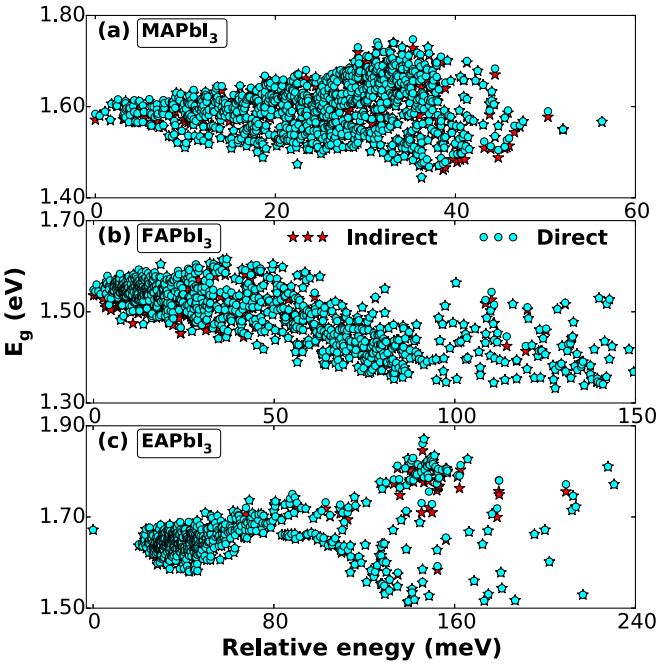

FIG. 3. Calculated band gaps using DFT-PBE functional for the (a) $MAPbI_3$, (b) $FAPbI_3$, and (c) $EAPbI_3$ as a function of the energy range when the molecules are evolved to rotate in the space.

varied within ~0.5 eV in cubic $MAPbI_3$ [31]. They also studied FA molecular dynamics in cubic $FAPbI_3$, estimating in this case band-gap changes ranging within 0.2 eV [44]. The plot in Fig. 3 shows a similar range of band-gap values obtained through the structure evolution process. It is clear that the molecular orientation can strongly influence the band gap of the hybrid perovskites by affecting the I-Pb-I inorganic framework which take part in the frontier orbitals. The PSO approach employed in our current study can efficiently overcome larger barriers in the potential energy landscape of these perovskites, and consequently provide an accurate estimate of the band-gap variation obtainable via molecular rotation and concerted octahedral tilting. Our results indicate band-gap values approximately ranging between 1.5–1.7 eV in $MAPbI_3$, 1.3–1.6 eV in $FAPbI_3$, and 1.5–1.9 eV in $EAPbI_3$.

Another impact of molecular rotation is small variations in k-space splitting (Rashba-type splitting) near the band edge that causes indirect gaps. This effect, reported in similar hybrid perovskites, [93–97], is a consequence of inversion symmetry breaking. This feature available among the hybrid materials may help suppress exciton formation and delay charge carrier recombination, which is essential for solar cell application [54]. All-inorganic perovskites such as $CsPbBr_3$ have direct band gap (~2.3 eV), and are known to luminesce with green excitonic emission in bulk or nanocrystalline forms [98,99]. The strength of Rashba-type splitting among hybrid perovskites can be approximately quantified via the Rashba parameter, $\alpha = 2\Delta E_R/\Delta k_R$, [100] where Δk is the momentum offset in k-space of the conduction band minimum (CBM) or valence band maximum (VBM) w.r.t the high symmetry k-point. It is shown for $MAPbI_3$ along R-Γ in Fig. 4(a). ΔE_R is the corresponding energy difference. The estimated α

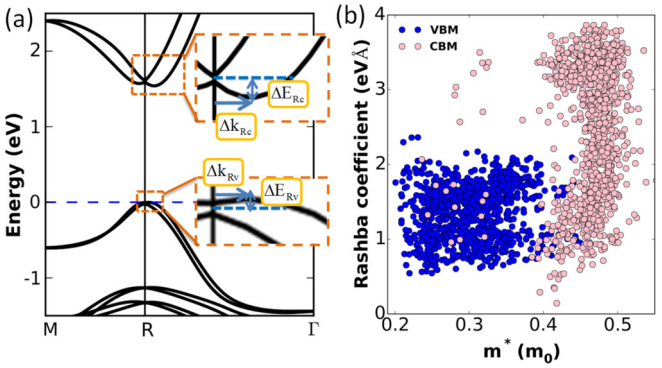

FIG. 4. (a) The illustration of the rashba splitting for the ground state of $MAPbI_3$ structures in the VBM and CBM and (b) calculated rashba coefficient with the energies of no more than 60 meV/f.u. higher than the ground state for the $MAPbI_3$ structures in the VBM ($\alpha_v = 2\,\Delta E_{Rv}/\Delta\, k_{Rv}$) and CBM ($\alpha_c = 2\,\Delta E_{Rc}/\Delta k_{Rc}$) along the high symmetry direction of the Brillouin zone R (0.5, 0.5, 0.5) $\rightarrow$ Γ (0.0, 0.0, 0.0) as a function of the effective mass. The calculations were done by using the DFT-PBE approach, including SOC.

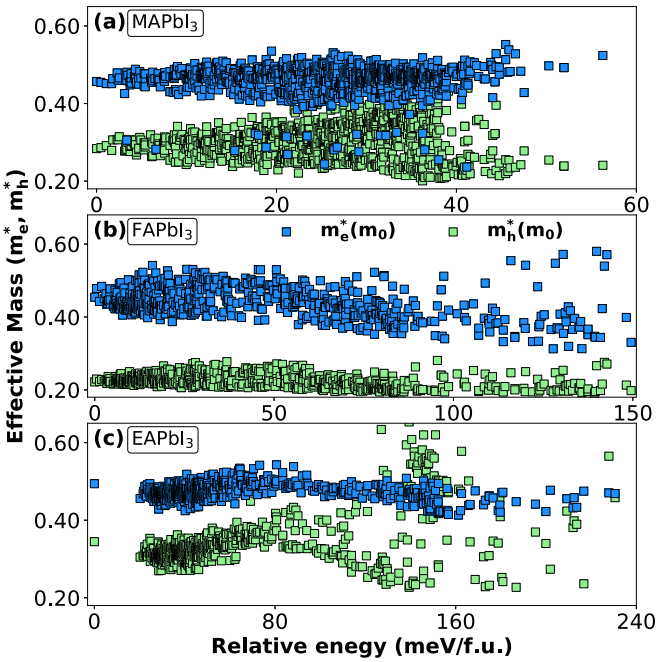

FIG. 5. Calculated effective mass of electron and hole using DFT-PBE functional for the (a) $MAPbI_3$, (b) $FAPbI_3$, and (c) $EAPbI_3$ as a function of the energy range with the evolution of the θ, ϕ, and ψ angles by rotating the molecules.

values of VBM/CBM in our predicted stable configurations of $MAPbI_3$, $FAPbI_3$ and $EAPbI_3$ are 1.16/2.64, 0.59/0.97, and 0.84/1.81 eVÅ, respectively. It is clear that Rashba parameters of the CBM are higher than those of the VBM in all three compounds, attributable to the spin-split Pb 6p orbitals that make up the conduction edge. Figure 4(b) depicts the Rashba parameters given as a function of calculated electron or hole effective mass for the different MA orientations obtained in the structure search of $MAPbI_3$. It indicates a wide range of achievable values of α, greater than those predicted earlier [101], approaching 4 eVÅ in the CBM and upto 2 eVÅ in the VBM. Hence, Rashba-type spin splitting caused by molecular reorientations may be one of the key features that help reduce charge carrier recombination and improve efficiency of hybrid perovskite-based solar cells [93,94,96].

Effective mass (m^*) tensors that relate directly to carrier's electrical conductivity are calculated using the PBE functional. Carrier effective masses of various structures as a function of relative energy w.r.t the most stable configuration are shown in Fig. 5. The electron masses (m_e^*) approximately range 0.4–0.6m_0 (m_0 being the electron rest mass) in all three compounds, and that of holes (m_h^*) between 0.2–0.4m_0 in $MAPbI_3$, 0.2-0.3m_0 in $FAPbI_3$, and 0.3-0.4m_0 in $EAPbI_3$. The results underscore variable m^* as the molecules are allowed to rotate within the Pb-I framework. Specific values of different $MAPbI_3$ structures along the kx, ky, and kz directions are shown in Fig. S3 [67]. The most stable configurations of $MAPbI_3$, $FAPbI_3$, and $EAPbI_3$ yield values of 0.29(0.26), 0.22(0.20), and 0.34(0.32)m_0 for the holes and 0.46(0.22), 0.47(0.27), 0.51(0.38)m_0 for electrons without(with) the SOC effect, respectively. For the three hybrid perovskites, the hole effective masses remain almost unaffected by the SOC, while the electron masses were uniformly overestimated by the DFT-PBE approach without the SOC. This is expected since the SOC mainly affects Pb-p orbitals dominating the conduction bands, but has no impact on the valence bands derived from Pb-s (where the relativistic Darwin effect causes the energy level upshift). The estimated effective mass of $MAPbI_3$ is in reasonable agreement with reported m_e^* of 0.35m_0 and m_h^* of 0.31 m_0 [102]. Low electron and hole effective masses due to the dispersive band edges contribute to the good, ambipolar electrical conductivity observed in experimental and theoretical calculations [8,56].

A notable aspect of Figs. 3 and 5 is the horizontal scale which represents the energy difference between the most stable and the least stable molecular orientations among the metastable (local minima) structures. It is about 60, 150, 240 meV/formula unit for $MAPbI_3$, $FAPbI_3$, and $EAPbI_3$, respectively (see Fig. S1), [67] indicating that the larger molecules rotate less freely and more slowly in the Pb-I framework. The figures also show the corresponding distribution in band gap and effective mass values with increasing energy of the structures.

We finally turn to the dielectric properties of the pseudocubic hybrid perovskite structures generated through our PSO search. As the orientation of the organic cations are allowed to change accompanied by octahedral tilting, the static dielectric constant values remain large. Anomalously high dielectric constant separates these ionic halides from traditional III-V and II-VI compound semiconductors. To evaluate the exciton binding energy E_B within the Wannier-Mott hydrogenic model, we use the calculated high frequency dielectric constant, ϵ_∞. The inverse relationship between E_B and dielectric constant for hybrid perovskites has been reported previously [103]. Figure 6 shows E_B as a function of calculated ϵ_∞, ranging between 50–110, 50–85, and 70–150 meV for different metastable states of the three different hybrid perovskites. These values are in overall agreement with experimental studies that have suggested low exciton binding energy, with few reporting values as low as 2 meV in the case

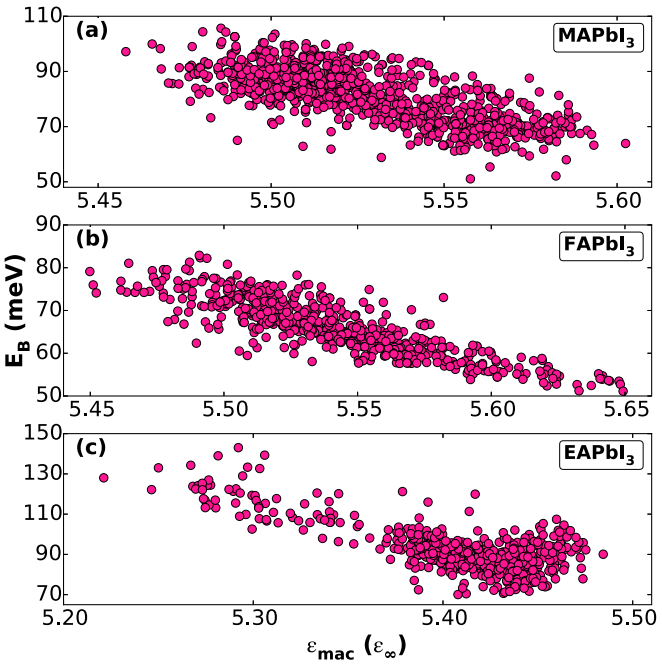

FIG. 6. Calculated exciton binding energies using DFT-PBE functional of the (a) $MAPbI_3$, (b) $FAPbI_3$, and (c) $EAPbI_3$, recpectively, as a function of the high-frequency limit of the dielectric constant.

of $MAPbI_3$ [12–19,21,23–25]. As the pseudocubic structure of the hybrid perovskites constantly evolve via molecular rotations, the exciton effective mass (not shown) and binding energy values remain consistently low. Considering that the exciton radii are large, either greater than or equal to the lattice constant, the electron-hole screened interaction is impacted by molecular rotations that cause local lattice polarization. We, thus, emphasize that reduced rate of bimolecular recombination among hybrid perovskites is a result of strong screening of electron-hole pairs by large static dielectric constant; a consequence of (local) lattice polarization caused by molecular rotations and induced octahedral tilting.

Finally, to simulate different equivalent alignments of organic molecules, we performed the calculations with the $2 \times 2 \times 2$ supercell of $MAPbI_3$, where for selected orientations (e.g., [001], [011], [012], [111]) the molecules are randomly aligned w.r.t. equivalent orientations. For each selected orientation, five configurations were constructed and the relevant properties such as total energy, band gap, carrier effective masses, and Rashba splitting coefficients were calculated. The results are shown in the supplementary Fig. S4 [67]. As seen, the fact that the [012] orientation of MA leads to the energetically most favorable structure is valid for all the configurations. The other properties such as band gap, carrier effective masses, and Rashba splitting coefficients show variation within a reasonably small range. These results indicate that the main findings discussed by using the unit cubic perovskite cell indeed are maintained when the larger supercell with different equivalent molecular orientations are used. It should be pointed out that we are not claiming a perfect correlation or alignment is expected throughout the entire volume of these hybrid perovskites. Rather, it emphasizes that a local microstructure is possible in these dynamical materials. The bulk crystal's response is an average over such microstructures which consist of preferred molecular orientations and corresponding octahedral distortions.

IV. CONCLUSION

We explored favored orientations of three different organic cations, viz., CH_3NH_3(MA), $CHNH_2NH_2$(FA), and $CH_3CH_2NH_3$(EA) inside the polyhedral cages of pseudocubic lead-halide perovskites and its impact on the electronic structure. Local metastable structures are searched by the particle swarm optimization algorithm combined with the first-principles DFT calculations. In the case of $MAPbI_3$, we find the [012] orientation of the MA cation to be most stable, separate from the commonly known [100], [110], and [111] orientations discussed in the literature. This study highlights the complex energy landscape formed by the metastable structures among hybrid preovskites and the effect of varying molecular orientations on their dynamical gap behavior, and Rashba splitting—both of which are connected to carrier generation and recombination that impact device performance. The dichotomy between predicted low effective mass of charge carriers and low-to-moderate carrier mobility has been a subject of debate. Deformation potential scattering by acoustic phonons, the possibility of large polarons, even strongly bound small polarons have been suggested as possible reasons for moderate mobility [104–108]. Our previous works described the possibility of electrostatic polarization caused by molecular reorientation that is indicative of long-range coupling, creating shallow trap-like states that bind charge carriers within a few kT of the CBM or VBM [109,110]. Current structure search indicates a similar phenomenon where molecular reorientations via three rotational degrees of freedom give rise to pseudocubic metastable structures, all of whom have low carrier effective mass. This finding is consistent with the view that at room or higher temperatures a global ground-state structure may be elusive as a result of organic rotation and octahedral tilting, whose phonon cloud "protect" the charge carrier by enhancing both its mass and lifetime. The crystal, however, maintains its average geometry. Additionally, we find that the exciton binding energy values remain consistently low among all searched structures. Thus, large exciton radius and strong screening may be the hallmarks of the hybrid perovskites that lead to reduced bimolecular pairing and efficient collection of photogenerated charge carriers.

ACKNOWLEDGMENTS

The work at Jilin University is supported by the National Natural Science Foundation of China (Grants No. 61722403 and 11674121), Jilin Province Science and Technology Development Program (Grant No. 20190201016JC), and the Program for Jilin University Science and Technology Innovative Research Team. K.B. acknowledges support from US Department of Homeland Security Grant Award Number 2014-DN-077-ARI075-05. Calculations were performed, in part, at the high performance computing center of Jilin University.

[1] *Best research-cell efficiencies*, https://www.nrel.gov/pv/assets/pdfs/pv-efficiency-chart.20190103.pdf.

[2] M. M. Lee, J. Teuscher, T. Miyasaka, T. N. Murakami, and H. J. Snaith, Science **338**, 643 (2012).

[3] Q. Xu, D. Yang, J. Lv, Y.-Y. Sun, and L. Zhang, Small Methods **2**, 1700316 (2018).

[4] X. Qin, Z. Zhao, Y. Wang, J. Wu, Q. Jiang, and J. You, J. Semicond. **38**, 011002 (2017).

[5] M. R. Filip, G. E. Eperon, H. J. Snaith, and F. Giustino, Nat. Commun. **5**, 5757 (2014).

[6] A. Kojima, K. Teshima, Y. Shirai, and T. Miyasaka, J. Am. Chem. Soc. **131**, 6050 (2009).

[7] S. De Wolf, J. Holovsky, S.-J. Moon, P. Löper, B. Niesen, M. Ledinsky, F.-J. Haug, J.-H. Yum, and C. Ballif, J. Phys. Chem. Lett. **5**, 1035 (2014).

[8] S. D. Stranks, G. E. Eperon, G. Grancini, C. Menelaou, M. J. P. Alcocer, T. Leijtens, L. M. Herz, A. Petrozza, and H. J. Snaith, Science **342**, 341 (2013).

[9] G. Xing, N. Mathews, S. Sun, S. S. Lim, Y. M. Lam, M. Grätzel, S. Mhaisalkar, and T. C. Sum, Science **342**, 344 (2013).

[10] D. Yang, W. Ming, H. Shi, L. Zhang, and M.-H. Du, Chem. Mater. **28**, 4349 (2016).

[11] Y. Wang, Y. Zhang, P. Zhang, and W. Zhang, Phys. Chem. Chem. Phys. **17**, 11516 (2015).

[12] A. Miyata, A. Mitioglu, P. Plochocka, O. Portugall, J. T.-W. Wang, S. D. Stranks, H. J. Snaith, and R. J. Nicholas, Nat. Phys. **11**, 582 (2015).

[13] Y. Yamada, T. Nakamura, M. Endo, A. Wakamiya, and Y. Kanemitsu, IEEE J. Photovolt. **5**, 401 (2015).

[14] K. Tanaka, T. Takahashi, T. Ban, T. Kondo, K. Uchida, and N. Miura, Solid State Commun. **127**, 619 (2003).

[15] V. D'Innocenzo, G. Grancini, M. J. Alcocer, A. R. S. Kandada, S. D. Stranks, M. M. Lee, G. Lanzani, H. J. Snaith, and A. Petrozza, Nat. Commun. **5**, 3586 (2014).

[16] S. Sun, T. Salim, N. Mathews, M. Duchamp, C. Boothroyd, G. Xing, T. C. Sum, and Y. M. Lam, Energy Environ. Sci. **7**, 399 (2014).

[17] M. Saba, M. Cadelano, D. Marongiu, F. Chen, V. Sarritzu, N. Sestu, C. Figus, M. Aresti, R. Piras, A. G. Lehmann, C. Cannas, A. Musinu, F. Quochi, A. Mura, and G. Bongiovanni, Nat. Commun. **5**, 5049 (2014).

[18] Q. Zhang, S. T. Ha, X. Liu, T. C. Sum, and Q. Xiong, Nano Lett. **14**, 5995 (2014).

[19] T. J. Savenije, C. S. Ponseca, Jr., L. Kunneman, M. Abdellah, K. Zheng, Y. Tian, Q. Zhu, S. E. Canton, I. G. Scheblykin, T. Pullerits, A. Yartsev, and V. Sundström, J. Phys. Chem. Lett. **5**, 2189 (2014).

[20] J. Song, J. Li, X. Li, L. Xu, Y. Dong, and H. Zeng, Adv. Mater. **27**, 7162 (2015).

[21] M. Hirasawa, T. Ishihara, T. Goto, K. Uchida, and N. Miura, Physica B: Condensed Matter **201**, 427 (1994).

[22] X. Li, Y. Wu, S. Zhang, B. Cai, Y. Gu, J. Song, and H. Zeng, Adv. Funct. Mater. **26**, 2435 (2016).

[23] A. M. Soufiani, Z. Yang, T. Young, A. Miyata, A. Surrente, A. Pascoe, K. Galkowski, M. Abdi-Jalebi, R. Brenes, J. Urban, N. Zhang, V. Bulović, O. Portugall, Y.-B. Cheng, R. J. Nicholas, A. Ho-Baillie, M. A. Green, P. Plochocka, and S. D. Stranks, Energy Environ. Sci. **10**, 1358 (2017).

[24] S. Tombe, G. Adam, H. Heilbrunner, D. H. Apaydin, C. Ulbricht, N. S. Sariciftci, C. J. Arendse, E. Iwuoha, and M. C. Scharber, J. Mater. Chem. C **5**, 1714 (2017).

[25] Z. Yang, A. Surrente, K. Galkowski, N. Bruyant, D. K. Maude, A. A. Haghighirad, H. J. Snaith, P. Plochocka-Maude, and R. J. Nicholas, J. Phys. Chem. Lett. **8**, 1851 (2017).

[26] W.-J. Yin, J.-H. Yang, J. Kang, Y. Yan, and S.-H. Wei, J. Mater. Chem. A **3**, 8926 (2015).

[27] M. H. Du, J. Mater. Chem. A **2**, 9091 (2014).

[28] W.-J. Yin, T. Shi, and Y. Yan, Appl. Phys. Lett. **104**, 063903 (2014).

[29] W. Ming, D. Yang, T. Li, L. Zhang, and M.-H. Du, Advanced Science **5**, 1700662 (2018).

[30] N. Onoda-Yamamuro, T. Matsuo, and H. Suga, J. Phys. Chem. Solids **51**, 1383 (1990).

[31] E. Mosconi, C. Quarti, T. Ivanovska, G. Ruani, and F. De Angelis, Phys. Chem. Chem. Phys. **16**, 16137 (2014).

[32] T. Glaser, C. Müller, M. Sendner, C. Krekeler, O. E. Semonin, T. D. Hull, O. Yaffe, J. S. Owen, W. Kowalsky, A. Pucci, and R. Lovrinčić, J. Phys. Chem. Lett. **6**, 2913 (2015).

[33] A. A. Bakulin, O. Selig, H. J. Bakker, Y. L. Rezus, C. Müller, T. Glaser, R. Lovrincic, Z. Sun, Z. Chen, A. Walsh, J. M. Frost, and T. L. C. Jansen, J. Phys. Chem. Lett. **6**, 3663 (2015).

[34] O. Selig, A. Sadhanala, C. Müller, R. Lovrincic, Z. Chen, Y. L. Rezus, J. M. Frost, T. L. Jansen, and A. A. Bakulin, J. Am. Chem. Soc. **139**, 4068 (2017).

[35] R. E. Wasylishen, O. Knop, and J. B. Macdonald, Solid State Commun. **56**, 581 (1985).

[36] O. Knop, R. E. Wasylishen, M. A. White, T. S. Cameron, and M. J. V. Oort, Can. J. Chem. **68**, 412 (1990).

[37] T. Baikie, N. S. Barrow, Y. Fang, P. J. Keenan, P. R. Slater, R. O. Piltz, M. Gutmann, S. G. Mhaisalkar, and T. J. White, J. Mater. Chem. A **3**, 9298 (2015).

[38] A. M. A. Leguy, J. M. Frost, A. P. McMahon, V. G. Sakai, W. Kochelmann, C. Law, X. Li, F. Foglia, A. Walsh, B. C. Ó'Regan, J. Nelson, J. T. Cabral, and P. R. F. Barnes, Nat. Commun. **6**, 7124 (2015).

[39] T. Chen, B. J. Foley, B. Ipek, M. Tyagi, J. R. Copley, C. M. Brown, J. J. Choi, and S.-H. Lee, Phys. Chem. Chem. Phys. **17**, 31278 (2015).

[40] K. Page, J. E. Siewenie, P. Quadrelli, and L. Malavasi, Angew. Chem. Int. Ed. **128**, 14532 (2016).

[41] I. P. Swainson, C. Stock, S. F. Parker, L. Van Eijck, M. Russina, and J. W. Taylor, Phys. Rev. B **92**, 100303(R) (2015).

[42] A. Mattoni, A. Filippetti, M. Saba, and P. Delugas, J. Phys. Chem. C **119**, 17421 (2015).

[43] M. A. Carignano, A. Kachmar, and J. Hutter, J. Phys. Chem. C **119**, 8991 (2015).

[44] C. Quarti, E. Mosconi, and F. D. Angelis, Phys. Chem. Chem. Phys. **17**, 9394 (2015).

[45] C. Quarti, E. Mosconi, and F. De Angelis, Chem. Mater. **26**, 6557 (2014).

[46] C. Quarti, E. Mosconi, J. M. Ball, V. D'Innocenzo, C. Tao, S. Pathak, H. J. Snaith, A. Petrozza, and F. De Angelis, Energy Environ. Sci. **9**, 155 (2016).

[47] A. Poglitsch and D. Weber, J. Chem. Phys **87**, 6373 (1987).

[48] Y. Kawamura, H. Mashiyama, and K. Hasebe, J. Phys. Soc. Jpn. **71**, 1694 (2002).

[49] H. Mashiyama, Y. Kurihara, and T. Azetsu, J. Korean Phys. Soc. **32**, S156 (1998).

[50] F. Brivio, A. B. Walker, and A. Walsh, APL Mater. **1**, 042111 (2013).

[51] J. M. Frost, K. T. Butler, and A. Walsh, APL Mater. **2**, 081506 (2014).

[52] J.-S. Park, S. Choi, Y. Yan, Y. Yang, J. M. Luther, S.-H. Wei, P. Parilla, and K. Zhu, J. Phys. Chem. Lett. **6**, 4304 (2015).

[53] M. T. Weller, O. J. Weber, P. F. Henry, A. M. D. Pumpo, and T. C. Hansen, Chem. Commun. **51**, 4180 (2015).

[54] C. Motta, F. El-Mellouhi, S. Kais, N. Tabet, F. Alharbi, and S. Sanvito, Nat. Commun. **6**, 7026 (2015).

[55] Y. Zhou, F. Huang, Y.-B. Cheng, and A. Gray-Weale, Phys. Chem. Chem. Phys. **17**, 22604 (2015).

[56] G. Giorgi, J.-I. Fujisawa, H. Segawa, and K. Yamashita, J. Phys. Chem. Lett. **4**, 4213 (2013).

[57] O. Yaffe, Phys. Rev. Lett. **118**, 136001 (2017).

[58] A. N. Beecher, O. E. Semonin, J. M. Skelton, J. M. Frost, M. W. Terban, H. Zhai, A. Alatas, J. S. Owen, A. Walsh, and S. J. L. Billinge, ACS Energy Lett. **1**, 880 (2016).

[59] Y. Chang, C. Park, and K. Matsuishi, J. Korean Phys. Soc **44**, 889 (2004).

[60] I. Borriello, G. Cantele, and D. Ninno, Phys. Rev. B **77**, 235214 (2008).

[61] G. E. Eperon, S. D. Stranks, C. Menelaou, M. B. Johnston, L. M. Herz, and H. J. Snaith, Energy Environ. Sci. **7**, 982 (2014).

[62] N. J. Jeon, J. H. Noh, W. S. Yang, Y. C. Kim, S. Ryu, J. Seo, and S. I. Seok, Nature **517**, 476 (2015).

[63] A. Mattoni, A. Filippetti, and C. Caddeo, J. Phys.: Condens. Matter **29**, 043001 (2016).

[64] J. M. Frost and A. Walsh, Acc. Chem. Res. **49**, 528 (2016).

[65] Y. Wang, J. Lv, L. Zhu, and Y. Ma, Phys. Rev. B **82**, 094116 (2010).

[66] Y. Wang, J. Lv, L. Zhu, and Y. Ma, Comput. Phys. Commun. **183**, 2063 (2012).

[67] See Supplemental Material at http://link.aps.org/supplemental/10.1103/PhysRevMaterials.3.125401 for (1) relative energy of predicted configurations as function of generation for the $FAPbI_3$ and $EAPbI_3$; (2) energy convergence test results with respect to the kinetic cutoff energy and k-point sampling for the three hybrid perovskites studied; (3) calculated average and diagonal components of electron and hole effective mass of $MAPbI_3$; (4) calculated total energy, band gap, carrier effective masses, and Rashba splitting coefficients for the selected molecular orientations in the $2\times2\times2$ supercell of $MAPbI_3$; (5) calculated lattice constants at different levels of theory, compared with the available experimental values of $MAPbI_3$; (6) calculated band gap using PBE and PBE+SOC functional of predicted stable $APbI_3$ (A = MA, FA and EA) with favorite orientation of C-N molecule; and (7) detailed structural information of predicted stable $APbI_3$ (A = MA, FA and EA) with favorite orientation of C-N molecule.

[68] M. T. Weller, O. J. Weber, J. M. Frost, and A. Walsh, J. Phys. Chem. Lett. **6**, 3209 (2015).

[69] J.-H. Im, J. Chung, S.-J. Kim, and N.-G. Park, Nanoscale Res. Lett. **7**, 353 (2012).

[70] G. Kresse and J. Furthmüller, Phys. Rev. B **54**, 11169 (1996).

[71] P. E. Blöchl, Phys. Rev. B **50**, 17953 (1994).

[72] J. P. Perdew, J. A. Chevary, S. H. Vosko, K. A. Jackson, M. R. Pederson, D. J. Singh, and C. Fiolhais, Phys. Rev. B **46**, 6671 (1992).

[73] J. P. Perdew, K. Burke, and M. Ernzerhof, Phys. Rev. Lett. **77**, 3865 (1996).

[74] D. A. Egger and L. Kronik, J. Phys. Chem. Lett. **5**, 2728 (2014).

[75] J.-H. Lee, N. C. Bristowe, P. D. Bristowe, and A. K. Cheetham, Chem. Commun. **51**, 6434 (2015).

[76] Y. Wang, T. Gould, J. F. Dobson, H. Zhang, H. Yang, X. Yao, and H. Zhao, Phys. Chem. Chem. Phys. **16**, 1424 (2013).

[77] J. Klimeš, D. R. Bowler, and A. Michaelides, J. Phys.: Condens. Matter **22**, 022201 (2010).

[78] A. V. Krukau, O. A. Vydrov, A. F. Izmaylov, and G. E. Scuseria, J. Chem. Phys. **125**, 224106 (2006).

[79] D. Yang, J. Lv, X. Zhao, Q. Xu, Y. Fu, Y. Zhan, A. Zunger, and L. Zhang, Chem. Mater. **29**, 524 (2017).

[80] G. K. Madsen and D. J. Singh, Comput. Phys. Commun. **175**, 67 (2006).

[81] C. C. Stoumpos, C. D. Malliakas, and M. G. Kanatzidis, Inorg. Chem. **52**, 9019 (2013).

[82] T. Baikie, Y. Fang, J. M. Kadro, M. Schreyer, F. Wei, S. G. Mhaisalkar, M. Graetzel, and T. J. White, J. Mater. Chem. A **1**, 5628 (2013).

[83] W. S. Yang, J. H. Noh, N. J. Jeon, Y. C. Kim, S. Ryu, J. Seo, and S. I. Seok, Science **348**, 1234 (2015).

[84] H. Zhou, Q. Chen, G. Li, S. Luo, T.-b. Song, H.-S. Duan, Z. Hong, J. You, Y. Liu, and Y. Yang, Science **345**, 542 (2014).

[85] D. P. McMeekin, G. Sadoughi, W. Rehman, G. E. Eperon, M. Saliba, M. T. Hörantner, A. Haghighirad, N. Sakai, L. Korte, B. Rech, M. B. Johnston, L. M. Herz, and H. J. Snaith, Science **351**, 151 (2016).

[86] D. Bi, W. Tress, M. I. Dar, P. Gao, J. Luo, C. Renevier, K. Schenk, A. Abate, F. Giordano, J.-P. C. Baena, J.-D. Decoppet, S. Mohammed Zakeeruddin, M. Khaja Nazeeruddin, M. Grätzel, and A. Hagfeldt, Sci. Adv. **2**, e1501170 (2016).

[87] Y. Yamada, T. Nakamura, M. Endo, A. Wakamiya, and Y. Kanemitsu, Appl. Phys. Express **7**, 032302 (2014).

[88] H.-S. Kim, C.-R. Lee, J.-H. Im, K.-B. Lee, T. Moehl, A. Marchioro, S.-J. Moon, R. Humphry-Baker, J.-H. Yum, J. E. Moser, M. Grätzel, and N.-G. Park, Sci. Rep. **2**, 591 (2012).

[89] S. Pang, H. Hu, J. Zhang, S. Lv, Y. Yu, F. Wei, T. Qin, H. Xu, Z. Liu, and G. Cui, Chem. Mater. **26**, 1485 (2014).

[90] T. M. Koh, K. Fu, Y. Fang, S. Chen, T. C. Sum, N. Mathews, S. G. Mhaisalkar, P. P. Boix, and T. Baikie, J. Phys. Chem. C **118**, 16458 (2014).

[91] N. Pellet, P. Gao, G. Gregori, T.-Y. Yang, M. K. Nazeeruddin, J. Maier, and M. Grätzel, Angew. Chem., Int. Ed. **53**, 3151 (2014).

[92] J. Li and P. Rinke, Phys. Rev. B **94**, 045201 (2016).

[93] A. Amat, E. Mosconi, E. Ronca, C. Quarti, P. Umari, M. K. Nazeeruddin, M. Grätzel, and F. De Angelis, Nano Lett. **14**, 3608 (2014).

[94] A. Stroppa, D. Di Sante, P. Barone, M. Bokdam, G. Kresse, C. Franchini, M.-H. Whangbo, and S. Picozzi, Nat. Commun. **5**, 5900 (2014).

[95] M. Kepenekian, R. Robles, C. Katan, D. Sapori, L. Pedesseau, and J. Even, ACS Nano **9**, 11557 (2015).
[96] T. Etienne, E. Mosconi, and F. De Angelis, J. Phys. Chem. Lett. **7**, 1638 (2016).
[97] Y. Zhai, S. Baniya, C. Zhang, J. Li, P. Haney, C.-X. Sheng, E. Ehrenfreund, and Z. V. Vardeny, Sci. Adv. **3**, e1700704 (2017).
[98] M. Sebastian, J. A. Peters, C. C. Stoumpos, J. Im, S. S. Kostina, Z. Liu, M. G. Kanatzidis, A. J. Freeman, and B. W. Wessels, Phys. Rev. B **92**, 235210 (2015).
[99] X. Zhang, H. Lin, H. Huang, C. Reckmeier, Y. Zhang, W. C. H. Choy, and A. L. Rogach, Nano Lett. **16**, 1415 (2016).
[100] D. Di Sante, P. Barone, R. Bertacco, and S. Picozzi, Adv. Mater. **25**, 509 (2013).
[101] L. Leppert, S. E. Reyes-Lillo, and J. B. Neaton, J. Phys. Chem. Lett. **7**, 3683 (2016).
[102] W.-J. Yin, T. Shi, and Y. Yan, Adv. Mater. **26**, 4653 (2014).
[103] J. Even, L. Pedesseau, and C. Katan, J. Phys. Chem. C **118**, 11566 (2014).
[104] H. Oga, A. Saeki, Y. Ogomi, S. Hayase, and S. Seki, J. Am. Chem. Soc. **136**, 13818 (2014).
[105] Q. Dong, Y. Fang, Y. Shao, P. Mulligan, J. Qiu, L. Cao, and J. Huang, Science **347**, 967 (2015).
[106] R. L. Milot, G. E. Eperon, H. J. Snaith, M. B. Johnston, and L. M. Herz, Adv. Funct. Mater. **25**, 6218 (2015).
[107] T. M. Brenner, D. A. Egger, A. M. Rappe, L. Kronik, G. Hodes, and D. Cahen, J. Phys. Chem. Lett. **6**, 4754 (2015).
[108] X.-Y. Zhu and V. Podzorov, J. Phys. Chem. Lett. **6**, 4758 (2015).
[109] B. Kang and K. Biswas, Phys. Chem. Chem. Phys. **19**, 27184 (2017).
[110] B. Kang and K. Biswas, J. Phys. Chem. C **121**, 8319 (2017).